 

# Macrodispersion in Generalized Sub-Gaussian randomly heterogeneous porous media

Laura Ceresa, Alberto Guadagnini, Monica Riva, Giovanni M. Porta

*Hydraulic Engineering Group, Department of Civil and Environmental Engineering, Politecnico di Milano, Piazza Leonardo Da Vinci 32, 20133 Milano, Italy.*

**Abstract**

In this work, we explore the implications of modeling the logarithm of hydraulic conductivity, $Y$, as a Generalized Sub-Gaussian (GSG) field on the features of conservative solute transport in randomly heterogeneous, three-dimensional porous media. Hydro-geological properties are often viewed as Gaussian random fields. Nevertheless, the GSG model enables us to capture documented non-Gaussian traits that are not explained through classical Gaussian models. Our formulation yields lead- (or first-) order analytical solutions for key statistical moments of flow and transport variables. These include flow velocities, hydraulic head, and macrodispersion coefficients, as obtained across GSG log-conductivity fields. The analytical model is based on a first-order spectral theory, which constrains the rigorous validity of our results to small values of log-conductivity variance ($\sigma_Y^2 << 1$). Analytical results are then compared against detailed numerical estimates obtained through a Monte Carlo scheme encompassing various levels of domain heterogeneity. An asymptotic Fickian transport regime is attained at late times in both Gaussian and GSG $Y$ fields. Convergence to such regime is slower for GSG as compared to Gaussian fields. This suggests a strong impact of the heterogeneity structure on non-Fickian pre-asymptotic behaviors of the kind documented in the literature. The quality of the comparison between analytical and numerical results deteriorates with

*Corresponding author
*Email address:* monica.riva@polimi.it (Monica Riva)

increasing $\sigma_Y^2$. Otherwise, our lead-order solutions frame macrodispersion coefficients in appropriate orders of magnitude also for values of $\sigma_Y^2$ up to approximately 1.7, which are consistent with the spatial variability of Y across a single geological unit. In this sense, our analytical approach enables one to obtain prior information on solute plume evolution and to grasp the effects of non-Gaussian medium heterogeneity while favoring simplicity. Our findings also enhance the current level of understanding of the nature of mass transfer across heterogeneous media characterized by complex variability structures which cannot be reconciled with classical Gaussian scenarios.

*Key words:*
Generalized Sub-Gaussian model, Hydrodynamic macrodispersion, Spectral theory, Heterogeneous hydraulic conductivity, Uncertainty quantification

## 1. Introduction

Analyses of fluxes of solute mass through heterogeneous subsurface porous media have been the subject of various studies. Their qualitative and quantitative assessment is relevant across several fields, such as energy engineering, hydrology, and Earth sciences. Characterization of the system evolution can be framed in terms of space-time distributions of solute concentrations. These are typically described by synthetic indicators which are representative of an effective behavior of the system [1, 2]. In this context, evaluation of trajectories of solute and fluid particles and patterns associated with solute plumes migrating across a target domain requires characterizing the underlying velocity field. This task is typically based on numerical solutions of a system of linearized governing differential equations (involving fluid-dynamics, solute, and heat transfer scenarios) associated with domains which can be very rarely approximated as homogeneous. The intrinsic spatial variability of the attributes of the host porous medium (e.g., permeability and porosity of natural subsurface reservoirs) prevents obtaining general closed-form analytical solutions describing the dynamics of quantities of interest such as space-time distributions of solute concentration.

| **Nomenclature of main symbols** | |
|---|---|
| Symbol | Quantity |
| $\boldsymbol{x}$ | position vector in a Cartesian system |
| $x_i$ | component of position vector along direction $i$ |
| $x_1$ | longitudinal (horizontal) position |
| $x_2$ | transverse (lateral) position |
| $x_3$ | transverse (vertical) position |
| $\boldsymbol{y}$ | second position vector in a Cartesian system |
| $y_i$ | component of second position vector along direction $i$ |
| $\boldsymbol{r}$ | separation or lag vector in a Cartesian system |
| $r_i$ | component of lag vector along direction $i$ |
| $r_1$ | longitudinal lag |
| $r_2$ | transverse (lateral) lag |
| $r_3$ | transverse (vertical) lag |
| $r$ | norm of $\boldsymbol{r}$ |
| $K$ | hydraulic conductivity |
| $K_G$ | geometric mean of hydraulic conductivity |
| $Y$ | log-conductivity |
| $\langle Y \rangle$ | ensemble expectation of $Y$ |
| $Y'$ | zero-mean random fluctuation of $Y$ around $\langle Y \rangle$ |
| $G(\boldsymbol{x})$ | multi-Gaussian random field |
| $U$ | subordinator |
| $\langle U \rangle$ | ensemble expectation of $U$ |
| $\langle U^2 \rangle$ | ensemble expectation of $U^2$ |
| $\sigma_Y^2$ | variance of $Y$ |
| $C_Y$ | covariance function of $Y$ |
| $I_Y$ | integral scale of $Y$ |
| $\sigma_G^2$ | variance of $G$ |
| $\rho_G$ | correlation function of $G$ |
| $C_G$ | covariance function of $G$ |
| $I_G$ | integral scale of $G$ |

| Nomenclature of main symbols | |
|---|---|
| Symbol | Quantity |
| $\alpha$ | shape parameter of log-normal $U$ |
| $\eta$ | parameter quantifying the departure of $Y$ from $G$ |
| $\boldsymbol{q}$ | Darcy flux |
| $h$ | hydraulic head |
| $\boldsymbol{u}$ | seepage velocity vector in a Cartesian system |
| $u_i$ | component of seepage velocity vector along direction $i$ |
| $\boldsymbol{k}$ | wave number vector in a Cartesian system |
| $k_i$ | component of wave number vector along direction $i$ |
| $k$ | norm of $\boldsymbol{k}$ |
| $\boldsymbol{X}$ | particle displacement in a Cartesian system |
| $X_i$ | particle displacement along direction $i$ |
| $\hat{C}_Y$ | spectrum of $C_Y$ |
| $C_h$ | hydraulic head covariance |
| $C_h^L$ | hydraulic head covariance along $r_1$ (longitudinal) |
| $C_h^T$ | hydraulic head covariance along $r_2$ or $r_3$ (transverse) |
| $\sigma_h^2$ | hydraulic head variance |
| $C_{u_i u_i}$ | diagonal entry of seepage velocity covariance tensor |
| $\hat{C}_h$ | spectrum of $C_h$ |
| $\hat{C}_{u_i u_i}$ | spectrum of $C_{u_i u_i}$ |
| $J$ | hydraulic gradient |
| $V$ | advective velocity modulus |
| $\phi$ | effective porosity |
| $t$ | time |
| $t^*$ | dimensionless travel time |
| $t_{ADV}$ | advective time |
| $t_0$ | initial (particle tracking) simulation time |
| $r_i^*$ | dimensionless lag component along direction $i$ |
| $C_{X_{ii}}$ | diagonal entry of displacement covariance tensor |
| $\boldsymbol{D}$ | macrodispersion tensor |

| **Nomenclature of main symbols** | |
|---|---|
| Symbol | Quantity |
| $D_{ii}$ | macrodispersion coefficient along direction $i$ |
| $L_{x_i}$ | size of numerical domain along direction $i$ |
| $s$ | numerical grid spacing |
| $\Delta t$ | time step for numerical particle tracking code |
| $\Delta r_1$ | average horizontal displacement in a time step |
| $N_P$ | number of particles |
| $N_S$ | number of Monte Carlo realizations |
| $\hat{t}_i^*$ | dimensionless travel time at which $D_{ii}$ |
| | achieves its asymptotic value |
| $\boldsymbol{x_{P_j}}$ | position vector of starting point considered |
| | to estimate $C_{X_{ii}}$ for particle $j$ numerically |
| $x_{iP_j}$ | component of $\boldsymbol{x_{P_j}}$ along direction $i$ |
| $x_{i,j,k}$ | spatial coordinate along direction $i$ |
| | of particle $j$ in numerical simulation $k$ |
| $X_{i,j,k}$ | displacement along direction $i$ |
| | of particle $j$ in numerical simulation $k$ |
| $\hat{\sigma}_{X_{i,j}}$ | displacement variance across the Monte Carlo |
| | sample (of particle $j$ along direction $i$) |
| $\hat{\sigma}_{X_{i,k}}$ | displacement variance across plume particles |
| | (along direction $i$ in simulation $k$) |
| $D_{ii}^{(ens)}$ | numerical ensemble macrodispersion along direction $i$ |
| $D_{ii}^{(eff)}$ | numerical effective macrodispersion along direction $i$ |

Characterization of spatial heterogeneities of natural subsurface reservoirs is always affected by uncertainties. These propagate from the stage of problem formulation (including model selection and ensuing parametrization) to modeling goals of interest [3–6]. When approached through numerical simulations, uncertainty quantification typically rests on a Monte Carlo framework and entails the need for large collections/ensembles of realizations [11, 13, 18]. This is in turn associated with large computational costs which might be somehow demanding from a data management and practical perspectives. The development of effective approaches capturing the effects associated with the interaction between solute mass transfer mechanisms and the structure of the underlying porous medium is then key to yield predictive tools that might find applications in diverse environmentally- and industrially-relevant scenarios.

Various approaches have been introduced to upscale transport features to a macroscopic scale resting on different conceptual, mathematical and operational frameworks [10, 13–16, 42]. In this study, we focus on the classical macrodispersive approach where the effect of system heterogeneity is addressed through the action of macrodispersion coefficients. The latter are conceptualized as attributes of the porous domain [1, 3, 12, 17, 18] in a way which is very similar to the case of thermal diffusivity. Thus, even as our study is keyed to mass transfer, the approach and strategy of analysis are readily transferable to settings entailing heat transfer in randomly heterogeneous porous media. Macrodispersion coefficients can be analytically derived starting from the statistics of the underlying hydraulic conductivity fields. These analytical solutions allow obtaining closed-form relationships that can be promptly used to interpret experimental observations and numerical simulation results related to heat and mass transfer in aquifer systems [12, 17, 20]. Moreover, an additional benefit associated with analytical approaches is that they enable one to rigorously benchmark numerically based results.

Here, our key objective is to develop and test novel analytical solutions associated with the characterization of macrodispersion in three-dimensional heterogeneous porous media. We do so upon relying on a stochastic approach according to which uncertainty in the spatial distribution of hydraulic conductivity is treated upon conceptualizing the system as a randomly heterogeneous field. With the aim of capturing key documented traits exhibited by empirical probability density functions (pdfs) of log-conductivity ($Y$) and its spatial increments in natural formations, a Generalized Sub-Gaussian (GSG) model has been introduced in [31] (its main traits are illustrated at the beginning of Section 2.1). This framework includes, as a particular case, the traditional approach based on viewing $Y$ as a Gaussian field. It is then markedly more flexible, as it enables one to readily accommodate the increasing amount of evidences that document scaling behaviors of the pdfs of spatial increments of $Y$ and other hydrogeological, geological, geophysical, and Earth science quantities [7, 22–30]. These evidences clearly demonstrate that the shape of the pdf associated with spatial increments of a variety of quantities (including, e.g., log-conductivity, porosity, or electrical resistivity) changes with the separation distance (or lag) at which increments are evaluated. In particular, it is noted that pdfs of increments display sharp peaks and heavy tails at short lags, these features tending to change (i.e., peaks decrease and tails become thinner) with increasing separation distances between locations at which increments are evaluated. Variance of the population of increments, which is directly related to the concept of variogram and spatial correlation, is also well known to change with lag. While the simultaneous occurrence of all of these traits is not consistent with an interpretation of $Y$ as a Gaussian random field, these are fully captured by the GSG theoretical framework of [31, 33].

Considering the above-mentioned body of evidences, our analysis rests on such a view, which ensures consistency in the joint stochastic representation of the random fields of $Y$ and its increments. In this context, we recall that even as well-established analytical solutions are available for macrodispersive coefficients in the presence of Gaussian distributions of $Y$ [1, 21], these approaches have not been yet systematically extended to GSG conductivity fields. Indeed, the vast majority of studies that document transport in heterogeneous porous media still relies on Gaussian models for the description of underlying $Y$ fields.

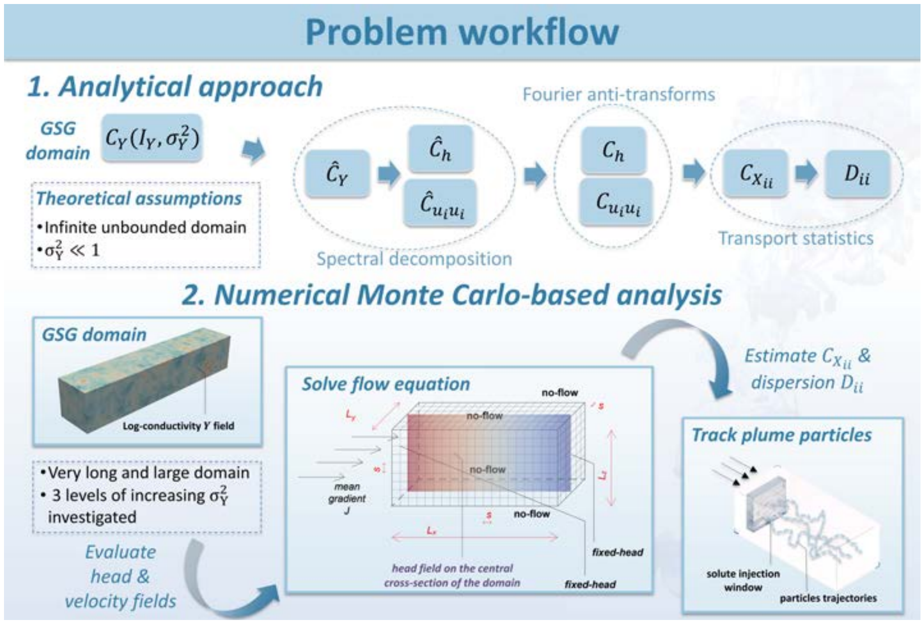


Figure 1: Workflow and sketch of the proposed approach.

Libera et al. [34] provide a first numerical study on the effect of a GSG distribution of $Y$ on concentration breakthrough curves at a well operating in a two-dimensional system. More recently, the role of the GSG nature of $Y$ on transport behavior has been explored in [18] through a detailed suite of numerical Monte Carlo simulations within a laboratory column. Analytical solutions depicting transport in two-dimensional GSG domains are presented in [32] and [19]. In this setting, the key distinctive element of the current study is the derivation of closed-form analytical expressions characterizing the behavior of main statistical quantities employed to describe subsurface flow and transport dynamics in three-dimensional GSG systems. Similar to the two-dimensional GSG scenarios analyzed in [32] and [19], we obtain lead- (or first-) order analytical solutions in the context of a perturbation approach. As the latter is based on a first-order approximation in terms of log-conductivity variance ($\sigma_Y^2$), our findings are rigorously valid for values of $\sigma_Y^2 << 1$. Therefore, we also assess in our study the potential of such lead-order solutions to be representative of systems with low to mild heterogeneity. We do so upon relying on a numerical Monte Carlo framework. In this context our first-order solution can be used to (i) obtain prior information in preliminary analyses of solute plume evolution and (ii) grasp the effects of (generally non-Gaussian) medium heterogeneity while favoring simplicity.

Our work is organized as follows. Section 2 addresses the methods. Section 2.1 describes the key theoretical elements and steps leading to the analytical expressions of the quantities of interest through first-order spectral methods, while Section 2.2 describes the setup and approach employed for our numerical analyses (see also Figure 1, where we illustrate the main methodological steps and we provide a sketch of the considered problem). Section 3 discusses key features of our analytical formulations and provides the comparison with numerical analogues for various levels of system heterogeneity. Section 4 summarizes the main findings of the work.

## 2. Methods

### *2.1. Analytical approach*

We consider steady-state uniform in the mean fully saturated groundwater flow taking place in a three-dimensional domain of infinite extent. The spatially heterogeneous log-conductivity field, $Y(\boldsymbol{x}) = \ln K(\boldsymbol{x})$ ($K$ denoting a spatial field of hydraulic conductivity and $\boldsymbol{x} = [x_1, x_2, x_3]$ being the position vector), is characterized through a GSG model. Here and in the following, the notation $Z'$ identifies a zero-mean random fluctuation of random process $Z$ around the ensemble mean $\langle Z \rangle$. Random fluctuations of $Y(\boldsymbol{x})$, i.e., $Y'(\boldsymbol{x}) = Y(\boldsymbol{x}) - \langle Y(\boldsymbol{x}) \rangle$, are modeled as $Y'(\boldsymbol{x}) = U(\boldsymbol{x})G(\boldsymbol{x})$, where $U(\boldsymbol{x})$ is a random positive subordinator and $G(\boldsymbol{x})$ is a zero mean multi-Gaussian random field. For the purpose of our analysis, we take the covariance function of $G(\boldsymbol{x})$ as isotropic, i.e., $C_G(r) = \sigma_G^2 \rho_G(r/I_G)$ ($\sigma_G^2$, $\rho_G$, and $I_G$ represent variance, correlation function, and integral scale of $G$, respectively; $r = |\boldsymbol{r}| = |\boldsymbol{x} - \boldsymbol{y}|$ denotes the norm of the separation vector $\boldsymbol{r} = [r_1, r_2, r_3]$ between two distinct locations $\boldsymbol{x}$ and $\boldsymbol{y}$). In this context, it has been shown [31] that the covariance $C_Y(r)$ of $Y$ is fully determined by $C_G(r)$ and the first two-orders statistical moments of $U$, according to:

$$C_Y(r) = \begin{cases} \sigma_G^2 \langle U \rangle^2 \rho_G({}^r/_{I_G}) & r > 0 \\ \sigma_Y^2 = \langle U^2 \rangle \sigma_G^2 & r = 0 \end{cases} . \tag{1}$$

Equation (1) reveals that the covariance of a GSG field always exhibits a nugget effect, which is therefore a distinctive feature of $Y$. The integral scale of $Y$ ($I_Y$) is always shorter than its counterpart ($I_G$) associated with the underlying Gaussian field, i.e.,:

$$I_Y = \frac{I_G}{\eta}, \text{ with } \eta = \frac{\langle U^2 \rangle}{\langle U \rangle^2} > 1. \tag{2}$$

In this work we take $\rho_G$ to be exponential, i.e., $\rho_G = e^{-\frac{r}{I_G}}$, so that Equation (1) can be expressed as:

$$C_Y(r) = \begin{cases} \frac{\sigma_Y^2}{\eta} e^{-\frac{r}{\eta I_Y}} & r > 0 \\ \sigma_Y^2 & r = 0 \end{cases} . \tag{3}$$

Note that the correlation structure of $Y$ is taken to be exponential for convenience of mathematical derivation. This does not constitute a basic assumption of the approach, which could be readily extended to other functional formats. Flow is driven by a constant average hydraulic gradient $J = -\langle \nabla h \rangle$ that is aligned with the longitudinal direction (here denoted through the positive direction of the coordinate axis $x_1$) and is governed by:

$$\nabla \cdot \boldsymbol{q} = 0; \quad \boldsymbol{q}(\boldsymbol{x}) = -K(\boldsymbol{x}) \nabla h(\boldsymbol{x}), \tag{4}$$

where $\boldsymbol{q}$ is the Darcy flux and $h$ is hydraulic head.

In the following, we develop analytical expressions for ($a$) hydraulic head covariance; ($b$) diagonal entries of the covariance matrix of seepage velocity $\boldsymbol{u}(\boldsymbol{x}) = {}^{\boldsymbol{q}(\boldsymbol{x})}/_{\phi}$, $\phi$ being the effective porosity, which is taken as a deterministic constant; ($c$) diagonal components of the covariance matrix of particle displacement $\boldsymbol{X}$; and ($d$) longitudinal and transverse components of the macrodispersion tensor.

Our theoretical framework rests on a first order spectral theory [21]. Accordingly, all of the above mentioned statistical moments can be evaluated starting from the three-dimensional spectral representation of Equation (3) [21, 35], hereafter denoted as $\hat{C}_Y(k)$, where $k = \sqrt{k_1^2 + k_2^2 + k_3^2}$ represents the magnitude of the wave number vector $\boldsymbol{k} = [k_1, k_2, k_3]$ in a Cartesian space (see also Figure 1 for a schematic representation of the main derivation steps). Details on the derivation of the spectrum (or spectral density) of $C_Y$ are included in the Supplementary Material A (see Equation (A.5)).

Spectra of longitudinal and transverse head covariance coincide and can be evaluated as [21]:

$$\hat{C}_h(k, k_1) = J^2 \frac{k_1^2}{k^4} \hat{C}_Y(k). \tag{5}$$

Spectra associated with the diagonal components of the covariance matrix of seepage velocities evaluated upon considering lags parallel to the mean flow direction $x_1$ can be computed as (see also [21]):

$$\hat{C}_{u_1 u_1}(k, k_1) = V^2 \frac{(k^2 - k_1^2)^2}{k^4} \hat{C}_Y(k), \tag{6}$$

$$\hat{C}_{u_i u_i}(k, k_1, k_i) = V^2 \frac{(k_i k_1)^2}{k^4} \hat{C}_Y(k), \text{ with } i = 2, 3, \tag{7}$$

where $V = \frac{K_G}{\phi} J$ is the magnitude of a macroscopic advective velocity, $K_G$ being the geometric mean of the hydraulic conductivity field.

Expressions for the covariance of hydraulic heads along directions parallel ($C_h^L$) and transverse ($C_h^T$) to the mean flow are derived in Supplementary Material B through the inverse Fourier transforms (in $\mathbb{R}^3$) of the spectrum provided in Equation (5), yielding:

$$\frac{C_h^L(r_1^*)}{J^2 \sigma_Y^2 I_Y^2} = \eta \left\{ \frac{8}{r_1^{*3}} - e^{-r_1^*} \left[ 1 + \frac{1}{r_1^*} \left( \frac{1}{4} + \frac{8}{r_1^*} \left( 1 + \frac{1}{r_1^*} \right) \right) \right] \right\}, \tag{8}$$

$$\frac{C_h^T(r_i^*)}{J^2 \sigma_Y^2 I_Y^2} = \frac{\eta}{r_i^*} \left\{ 1 - \frac{4}{r_i^{*2}} + e^{-r_i^*} \left[ 1 + \frac{4}{r_i^*} \left( 1 + \frac{1}{r_i^*} \right) \right] \right\}, \text{ with } i = 2, 3, \tag{9}$$

where $r_i^* = {r_i}/{(\eta I_Y)}$. Considering Equations (8) and (9) (see also the Supplementary Material B), the head variance, $\sigma_h^2$, reads:

$$\frac{\sigma_h^2}{J^2 \sigma_Y^2 I_Y^2} = \frac{\eta}{3}. \tag{10}$$

Following a similar procedure, it can be shown (see the Supplementary Material C for details) that the diagonal entries of the covariance matrix associated with seepage velocity components (i.e., $C_{u_1u_1}$ and $C_{u_iu_i}$, with $i = 2, 3$) evaluated at separation distances $r_1^*$ along the mean flow direction are given by:

$$\frac{C_{u_1u_1}(r_1^*)}{V^2\sigma_Y^2} = 8\begin{cases} \dfrac{1}{\eta r_1^{*2}}\Bigg\{\dfrac{1}{r_1^*} - \dfrac{12}{r_1^{*3}} \\ \qquad + e^{-r_1^*}\left[1 + \dfrac{1}{r_1^*}\left(5 + \dfrac{12}{r_1^*}\left(1 + \dfrac{1}{r_1^*}\right)\right)\right]\Bigg\} & r_1^* > 0 \\ \dfrac{1}{15} & r_1^* = 0 \end{cases}, \tag{11}$$

$$\frac{C_{u_iu_i}(r_1^*)}{V^2\sigma_Y^2} = \begin{cases} \dfrac{1}{\eta r_1^{*}}\Bigg\{-\dfrac{2}{r_1^{*2}} + \dfrac{48}{r_1^{*4}} \\ \qquad - e^{-r_1^*}\left[1 + \dfrac{2}{r_1^*}\left(3 + \dfrac{1}{r_1^*}\left(11 + \dfrac{24}{r_1^*}(1 + \dfrac{1}{r_1^*})\right)\right)\right]\Bigg\} & r_1^* > 0 \\ \dfrac{1}{15} & r_1^* = 0 \end{cases}$$

$$\text{with } i = 2, 3. \tag{12}$$

Note that Equations (11) and (12) are clearly characterized by the presence of a nugget effect, this feature being otherwise not displayed by the head covariance (see Equations from (8) to (10) and the Supplementary Material C). This behavior is mirrored also in the two-dimensional scenario previously analyzed by Riva et al. [32].

The directional components of the covariance matrix associated with particle displacement, i.e., $C_{X_{ii}}$, evaluated at lags oriented along the longitudinal direction can be derived as [1]:

$$C_{X_{ii}}(r_1) = \frac{2}{V^2}\int_0^{r_1}(r_1 - z)C_{u_iu_i}(z)dz, \text{ with } i = 1, 2, 3. \tag{13}$$

Replacing Equations (11) and (12) into Equation (13), respectively, leads to:

$$\frac{C_{X_{11}}(r_1^*)}{I_Y^2\sigma_Y^2} = 8\eta\left\{\frac{1}{r_1^*} - \frac{2}{r_1^{*3}} - \frac{2}{3} + \frac{1}{4}r_1^* + \frac{2e^{-r_1^*}}{r_1^{*2}}\left(1 + \frac{1}{r_1^*}\right)\right\} \tag{14}$$

$$\frac{C_{X_{ii}}(r_1^*)}{I_Y^2\sigma_Y^2} = 2\eta\left\{-\frac{1}{r_1^*} + \frac{4}{r_1^{*3}} + \frac{1}{3} - \frac{e^{-r_1^*}}{r_1^*}\left[1 + \frac{4}{r_1^*}\left(1 + \frac{1}{r_1^*}\right)\right]\right\}, \text{ with } i = 2, 3. \tag{15}$$

Following Gelhar [21], the diagonal components of the macrodispersion tensor $\boldsymbol{D}$ evaluated along direction $i$ at (longitudinal) lags can be expressed as:

$$D_{ii}(r_1) = \int_0^{r_1} C_{u_i u_i}(\varrho) d\varrho, \text{ with } i = 1, 2, 3. \tag{16}$$

Making use of Equations (11), (12) and (16), normalized longitudinal and transverse macrodispersion coefficients become, respectively:

$$\frac{D_{11}(t^*)}{V I_Y \sigma_Y^2} = 1 - \frac{4\eta^2}{t^{*2}} + \frac{24\eta^4}{t^{*4}} - \frac{8\eta^2}{t^{*2}} e^{-\frac{t^*}{\eta}} \left[1 + \frac{3\eta}{t^*}\left(1 + \frac{\eta}{t^*}\right)\right] \tag{17}$$

$$\frac{D_{ii}(t^*)}{V I_Y \sigma_Y^2} = \frac{\eta}{t^*}\left\{\frac{\eta}{t^*} - \frac{12\eta^3}{t^{*3}} + e^{-\frac{t^*}{\eta}}\left[1 + \frac{\eta}{t^*}\left(5 + \frac{12\eta}{t^*}\left(1 + \frac{\eta}{t^*}\right)\right)\right]\right\}, \text{ with } i = 2, 3. \tag{18}$$

Here, $t^*$ denotes the dimensionless format of travel time $t$, which is normalized against the characteristic advective time $t_{ADV} = {}^{I_Y}/_{V}$. The latter represents the time taken by one particle to travel a distance equal to $I_Y$ (by advection). As the advective velocity is purely longitudinal in our settings, such displacement is fully along the direction parallel to the axis $x_1$. Accordingly, dimensionless travel time $t^*$ can be written as:

$$t^* = \frac{t}{t_{ADV}} = \frac{r_1}{I_Y} = \eta r_1^*. \tag{19}$$

### *2.2. Numerical approach and setup for validation*

The lead-order analytical results illustrated in Section 2.1 are theoretically constrained by a low heterogeneity level of the system (e.g., [1, 21]), i.e., $\sigma_Y^2 << 1$. Here, we assess the consistency of these results for various levels of heterogeneity (in terms of $\sigma_Y^2$) through comparisons against a suite of detailed numerical Monte Carlo simulations performed across a three-dimensional domain (see also Figure 1 for a schematic illustration of the numerical approach). Note that the smallest $\sigma_Y^2$ value considered in our study has been selected to validate our numerical model (i.e., it is sufficiently low to completely fulfill the assumption $\sigma_Y^2 << 1$; see also Section 3.2). Following Riva et al. [32], the subordinator associated with the GSG model describing the heterogeneous spatial distribution of $Y$ is taken as log-normal, i.e., $U(\boldsymbol{x}) \sim \ln N(0, (2-\alpha)^2)$, where the shape parameter $\alpha < 2$ governs the deviation of the probability density function of $Y$ from Gaussian. Note that the GSG distribution tends to become Gaussian when $\alpha \to 2$. In this context, the following relationships hold [31]:

$$\eta = e^{(2-\alpha)^2},\ \sigma_Y^2 = e^{2(2-\alpha)^2}\sigma_G^2,\ I_Y = e^{-(2-\alpha)^2} I_G. \tag{20}$$

Our numerical Monte Carlo simulations are then based on selecting $\alpha = 1.5$ (i.e., corresponding to $\eta = 1.284$, so that the Sub-Gaussian nature of the $Y$ field is appreciable), and are showcased for various degrees of spatial heterogeneity, as detailed in the following. Multiple unconditional realizations of the $Y$ fields are generated according to the approach illustrated in [36]. Groundwater flow is then evaluated on the resulting $Y$ realizations. We do so by considering the three-dimensional setting depicted in Figure 2 and characterized by a longitudinal and transverse sizes equal to $L_{x_1} = 300$ m and $L_{x_i} = 70$ m (with $i = 2, 3$), respectively, and discretized with a uniform grid of spacing $s = 1$ m (i.e., the domain is formed by 1.4 millions of cells). Mean uniform flow conditions are ensured through a constant head drop between the two vertical planes located at $x_1 = 0$ and $x_1 = L_{x_1}$. This yields an overall head gradient $J = 2.5 \cdot 10^{-3}$, the remaining domain boundaries being considered as impervious.

We set $\phi = 10\%$, $K_G = 10^{-2}$ m/s and $I_G = 7$ m (i.e., $I_Y \approx 5.5$ m), which yields

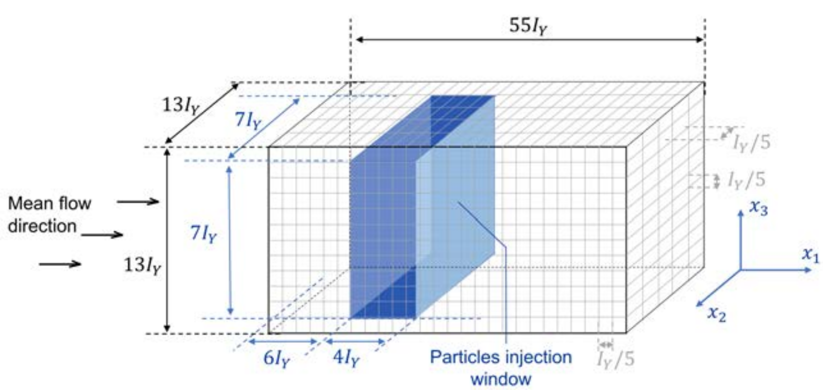


Figure 2: Simulation domain and particles injection window.

${}^{L_{x_1}}/_{I_Y} \approx 55$ and ${}^{L_{x_i}}/_{I_Y} \approx 13$ (for $i = 2, 3$). We have verified that the numerical solution is not significantly affected by the boundary conditions at distances of approximately $6I_Y$ from the inlet/outlet and $3I_Y$ from the no-flow boundaries (see also Section 3.2). Three families of random fields are explored. These are associated with increasing levels of heterogeneity, as expressed through $\sigma_G^2 = 0.001, 0.500$, and $1.000$ and corresponding to $\sigma_Y^2 = 1.648 \cdot 10^{-3}, 8.244 \cdot 10^{-1}$, and 1.648, respectively. These values are deemed as representative of various degrees of natural variability contained within a geological unit (see, e.g., [43] and references therein), which can potentially be depicted through statistically stationary heterogeneous models of the kind we consider here. Appreciably larger values of $\sigma_Y^2$ are otherwise recognized to stem from a homogenization of conductivity values pertaining to diverse geological facies within a unique population (e.g., [39]).

Flow is evaluated upon relying on an in-house, well tested, open-source code that employs a diagonally preconditioned Conjugate Gradient solver for symmetric matrices in compressed sparse row matrix format. It is here noticed that the selected mesh yields a satisfactory compromise between computational efforts and an acceptable reproduction of the spatial heterogeneity in each realization across which transport simulations are performed. In this sense, the resulting 5 elements per correlation scale of the grid where $Y$ is generated are typically viewed as an acceptable trade-off [40].

We solve purely advective solute transport by way of a particle tracking algorithm that is implemented according to a uniform temporal discretization scheme. The selected time step is $\Delta t = 12500$ s, which corresponds to ${}^{\Delta r_1}/_{I_Y}$ roughly equal to 0.5, $\Delta r_1$ being the longitudinal displacement that is accomplished on average by each particle in a single time step. Preliminary convergence tests showed that our choice guarantees a satisfactory approximation of (average) particles trajectories in relationship with the main purposes of our study (i.e., the numerical evaluation of key ensemble moments of the transport problem; details not shown).

Particles are initially randomly distributed within the blue volume depicted in Figure 2. Tracking a number of $N_P = 1000$ particles across the domain enables us to obtain stable results in terms of the quantities analyzed in Section 3.2 for each Monte Carlo realization of $Y$. The computational flow and transport simulation time is approximately 10 minutes for each Monte Carlo realization on a 40 system cores-based machine with 2 x Intel Xeon Gold 6148 CPU and 192 GB RAM.

## 3. Results and Discussion

### 3.1. Analytical results

This Section is devoted to the presentation and discussion of the analytical expressions reported in Section 2.1. Statistical flow and transport moments are illustrated in Figure 3 for three values of $\eta$, i.e., $\eta = 1.284, 1.041,$ and $1.000$. These correspond to $\alpha = 1.5, 1.8,$ and $2$, respectively, the latter value representing the setting associated with a Gaussian $Y$ field. The analysis of the scenario corresponding to $\eta = 1.041$ (i.e., $\alpha = 1.8$) enables us to enrich the range of degrees of departure of $Y$ from Gaussian and is consistent with the corresponding study performed in [32] for two-dimensional settings.

Figure 3a depicts the behavior of hydraulic head covariance at increasing dimensionless lag evaluated according to Equations (8) and (9). Head covariances along longitudinal and transverse directions display similar trends. The rate at which head correlation decreases is higher along the longitudinal direction, while transverse head covariance is still sustained at more than 20 integral scales of $Y$. The latter trait is consistent with the nature of the flow scenario investigated according to which pressure head is uniform (on average) along the transverse direction. Figure 3a also evidences that head covariance obtained in GSG fields (regardless lag orientation and magnitude) is always larger than its Gaussian counterpart (corresponding to $\eta = 1$). This clearly indicates that Sub-Gaussianity strengthens the correlation degree exhibited by hydraulic heads

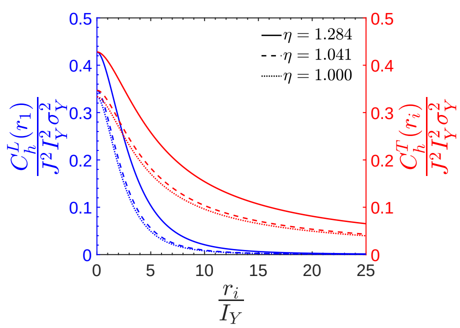


(a)

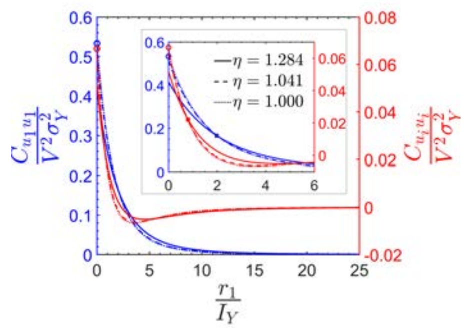


(b)

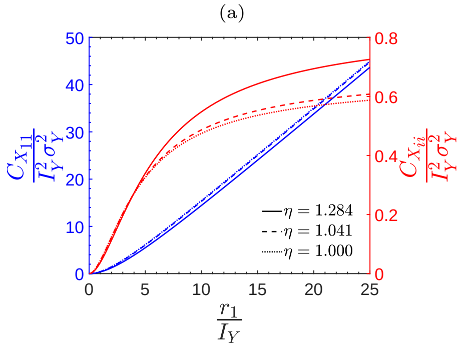


(c)

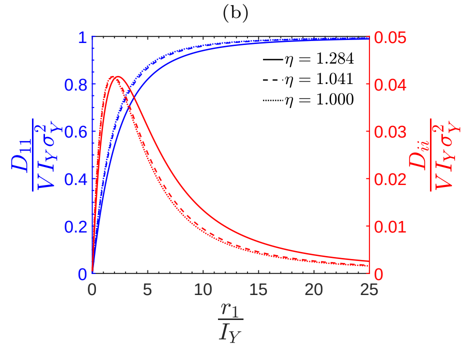


(d)

Figure 3: (a) Directional head covariance, (b) diagonal components of seepage velocity covariance, (c) diagonal components of particle displacement covariance, (d) directional macrodispersion coefficients. Blue and red curves refer to longitudinal (i.e., $i = 1$) and transverse directions (i.e., $i = 2, 3$), respectively.

within the considered domain.

Figure 3b depicts the behavior of the diagonal components of the velocity covariance tensor, which are evaluated according to Equations (11) and (12). Both longitudinal and transverse velocity covariances are seen to exhibit a clear nugget effect at the origin (zero lag), which becomes more pronounced at increasing values of $\eta$ and vanishes in the Gaussian case. The covariance of the transverse velocity component displays a behavior characterized by a hole effect. This feature was also observed in the presence of a Gaussian $Y$ field (e.g., [1] and [21]) and is still preserved in the non-Gaussian setting here analyzed. Note that Figure 3b also embeds an insert which is focused on early times (i.e., short distances) and enables to see that covariance curves intersect each other (see the symbols marking such intersection in the insert). This feature was also observed in [32] for a two-dimensional case at distances of about $3I_Y$. Here, it is noted to take place at shorter distances (i.e., around $(0.5-2)I_Y$, depending on the direction). This corresponds to an inversion experienced in the relative strength of directional velocity covariances associated with Sub-Gaussian and Gaussian $Y$ fields. GSG fields induce a weaker velocity correlation than their Gaussian counterparts at very short distances, (i.e., for $r_1/I_Y \leq 0.5-2$). Otherwise, we find an opposite situation at larger distances, i.e., where velocity correlation is more persistent in GSG than in Gaussian fields.

Figure 3c depicts the behavior of longitudinal and transverse covariances associated with directional particle displacements, these quantities being evaluated according to Equations (14) and (15). Figure 3d displays normalized macrodispersions evaluated by Equations (17) and (18). Longitudinal particle displacement covariance displays a monotonic growth with lag. At early times/small lags, the dependence on $r_1/I_Y$ is quadratic, $\lim_{\frac{r_1}{I_Y}\to 0} C_{X_{11}} = \frac{8I_Y^2\sigma_Y^2}{15\eta}(\frac{r_1}{I_Y})^2$, in agreement with the behavior observed in [1] for Gaussian $Y$ fields. At late times/large separation distances, $C_{X_{11}}$ becomes a linear function of the dimensionless travel distance, $\lim_{\frac{r_1}{I_Y}\to\infty} C_{X_{11}} = 2I_Y^2\sigma_Y^2(\frac{r_1}{I_Y} - \frac{8\eta}{3})$, a feature that is documented also in the Gaussian case [1]. These observations are consistent with the behavior exhibited by the longitudinal macrodispersion (see Figure

3d), where $D_{11}$ is seen to linearly grow during the pre-asymptotic regime (i.e., when $C_{X_{11}} \propto (r_1/I_Y)^2$) to then attain a horizontal plateau at late times (i.e., when $C_{X_{11}} \propto r_1/I_Y$). The transition towards the latter condition, which is often referred to as asymptotic or Fickian macrodispersion regime, is also observed for transverse macrodispersion (see Figure 3d). The latter is seen to peak during the pre-asymptotic regime to then decay to zero, this behavior being consistent with that of transverse particle displacement covariance (see Figure 3c). Specifically, $C_{X_{ii}}$ (with $i = 2, 3$) is a quadratic function of $r_1/I_Y$ at short lags ($\lim_{\frac{r_1}{I_Y}\to 0} C_{X_{ii}} = \frac{I_Y^2 \sigma_Y^2}{15\eta}(\frac{r_1}{I_Y})^2$), whereas, it reaches a horizontal asymptote at late times ($\lim_{\frac{r_1}{I_Y}\to 0} C_{X_{ii}} = \frac{2}{3}\eta I_Y^2 \sigma_Y^2$), analogous features being documented for the classical Gaussian case [1]. The sharp peak experienced by transverse macrodispersion even in the absence of pore scale diffusion has already been interpreted for classical Gaussian fields as a macroscale scale effect of the domain heterogeneity [38]. In this sense, some particles are forced to depart from the average trajectory in the attempt to overcome low conductivity regions. This heterogeneity-induced twiggling and intertwinning effect (as also noted in [38]) is responsible for the transverse spread experienced by the plume also in Sub-Gaussian fields. This effect becomes increasingly pronounced as the domain becomes more heterogeneous. It is also noticed that the peak of $D_{ii}$ (with $i = 2, 3$) is significantly lower in the three-dimensional setting as compared against its two-dimensional counterpart [32] (given the same values of $I_Y$ and $\sigma_Y^2$). This is related to the observation that particles can spread more freely in three- than in two- dimensional systems.

Figure 3d clearly shows that an increased departure of $Y$ from the Gaussian scenario (i.e., increasing values of $\eta$) yields a longer delay which is experienced by longitudinal and transverse macrodispersion curves to reach an asymptotic transport regime. Otherwise, non-Gaussian features of $Y$ do not impact the asymptotic values attained by longitudinal and transverse macrodispersion.

The duration of pre-asymptotic regimes observed in our scenarios can be quantified introducing a characteristic time $\hat{t}_i^*$ defined as the dimensionless time $(t/t_{ADV})$ at which the normalized macrodispersion coefficient, $D_{ii}/(V I_Y \sigma_Y^2)$ , approaches its late time asymptote (equal to 1 when $i = 1$ and to 0 for $i = 2, 3$). Accordingly, $\hat{t}_1^*$ is defined as the dimensionless time at which $D_{11}/(VI_Y\sigma_Y^2)$ achieves the value of 0.99, whereas $\hat{t}_2^*$ (or $\hat{t}_3^*$) is defined as the dimensionless late time at which $D_{22}/(VI_Y\sigma_Y^2)$ (or $D_{33}/(VI_Y\sigma_Y^2)$) becomes negligible. The latter condition is considered to be attained when $D_{22}/(VI_Y\sigma_Y^2)$ (or $D_{33}/(VI_Y\sigma_Y^2)$) reaches 1% of its maximum value. As shown in Figure 4, $\hat{t}_i^*$ increases with $\eta$, i.e., the extent of the pre-asymptotic transport regime along longitudinal and transverse directions increases with the departure of $Y$ from classical Gaussian scenarios.

The results presented so-far evidence that the departure from Gaussianity does not affect the extent to which directional spreading of the plume acts at late times, but has a marked influence on the pre-asymptotic behavior. This suggests that GSG effects on transport may be apparent when considering pre-asymptotic (non-Fickian) conditions and may vanish at asymptotic regimes. The shift towards larger distances experienced by the peak of transverse macrodispersion and the attainment of an horizontal plateau for $D_{11}$ within Sub-Gaussian fields are also consistent with the trends exhibited by directional displacement covariances. The results obtained on the covariance of particle displacements suggest that adopting a GSG model is likely to have a relevant influence on mixing metrics. The assessment of these effects is beyond the objective of this study and will be considered in future works.

### *3.2. Comparison between numerical Monte Carlo results and analytical solutions*

We illustrate here the comparisons of the (Monte Carlo-based) numerical results associated with particle displacement covariances and directional macrodispersions against the corresponding (perturbation-based) analytical solutions presented in Section 2.1 and discussed in Section 3.1. The stability of these results is verified to be attained for a minimum number ($N_S$) of Monte Carlo simulations which increases with the degree of system heterogeneity (i.e., $N_S \approx 1500, 2000, 4000$ are required for $\sigma_Y^2 = 1.684 \cdot 10^{-3}, 8.244 \cdot 10^{-1}, 1.648$, respectively; details not shown). For consistency, all of the results we illustrate in the

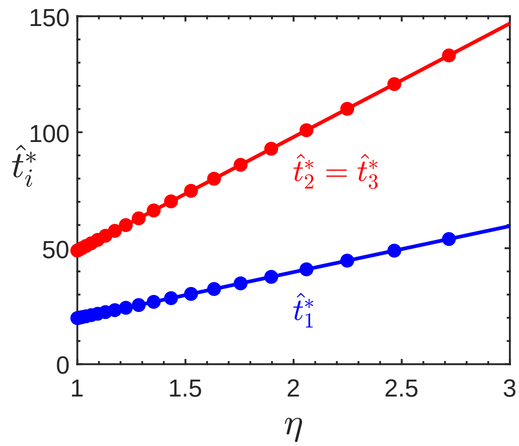


Figure 4: Dimensionless travel time $\hat{t}_i^*$ versus $\eta$.

following are based on $N_S = 5000$. The three levels of domain heterogeneity are selected according to the following rationale: (i) results associated with the lowest value of $\sigma_Y^2$ (i.e., $1.684 \cdot 10^{-3} << 1$) can be employed to test the accuracy of our numerical schemes when compared against the analytical outcomes; (ii) the remaining two values of $\sigma_Y^2$ are designed to assess the accuracy of the analytical solution at increasing levels of domain heterogeneity.

Figure 5 depicts numerical and analytical results related to the covariance functions $C_{X_{ii}}$ versus $^{r_1}/_{I_Y}$ (with $i = 1, 2, 3$). Numerical estimates of $C_{X_{ii}}$ are computed according to:

$$C_{X_{ii}}(r_1) = \frac{1}{N_P} \sum_{j=1}^{N_P} \Bigg[ \frac{1}{N_S} \sum_{k=1}^{N_S} \bigg( X_{i,j,k}(x_{1P_j}, x_{2P_j}, x_{3P_j}) - \frac{1}{N_S} \sum_{k=1}^{N_s} X_{i,j,k}(x_{1P_j}, x_{2P_j}, x_{3P_j}) \bigg)$$
$$\bigg( X_{i,j,k}(x_{1P_j} + r_1, x_{2P_j}, x_{3P_j}) - \frac{1}{N_S} \sum_{k=1}^{N_s} X_{i,j,k}(x_{1P_j} + r_1, x_{2P_j}, x_{3P_j}) \bigg) \Bigg]$$
$$\text{with } \boldsymbol{x_{P_j}} \text{ fixed } \forall j, k; \quad i = 1, 2, 3, \tag{21}$$

where $\boldsymbol{x_{P_j}} = [x_{1P_j}, x_{2P_j}, x_{3P_j}]$ represents the starting point for the evaluation of $C_{X_{ii}}$ (corresponding to zero lag), i.e., the initial position of particle $j$ in the injection window highlighted in Figure 2. The displacement along direction $i$ of particle $j$ in Monte Carlo simulation $k$ is defined as $X_{i,j,k}(t) = x_{i,j,k}(t) - x_{i,j,k}(t_0 = 0)$, where $t_0$ denotes the initial time (i.e., when particles are released in the domain depicted in Figure 2) and $x_{i,j,k}$ represents the spatial coordinate of particle $j$ in simulation $k$, along direction $i$ at time $t$ ($t$ being directly related to $r_1$ according to Equation (19)). Figure 5 documents a satisfactory agreement between

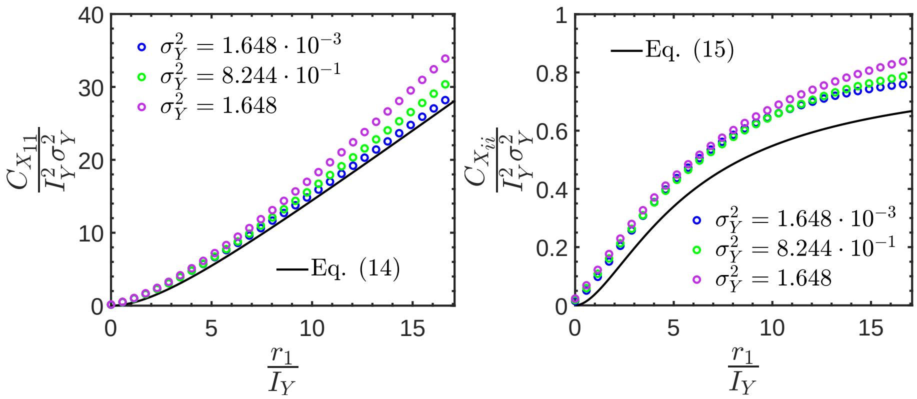


(a) (b)

Figure 5: Covariance of (a) longitudinal (i.e., along direction $i = 1$) and (b) transverse (i.e., along directions $i = 2, 3$) particle displacements. Analytical and numerical solutions are depicted with solid curves and colored circles, respectively.

numerical and analytical solutions of $C_{X_{ii}}$. As expected, differences between numerical and analytical results increase with $\sigma_Y^2$. The accuracy of numerical estimates of $C_{X_{ii}}$ at low degrees of domain heterogeneity ($\sigma_Y^2 = 1.684 \cdot 10^{-3}$) is slightly higher along the longitudinal direction. This aspect is ascribed to the relatively small size (in terms of integral scales of $Y$) of the domain along the transverse directions, which might impact on particle displacement in a way which is slightly stronger than along the longitudinal one. Given the consistency and good quality of all results, however, our domain choice is justified by the achievement of a satisfactory trade-off between high numerical accuracy and extremely high computational costs (note that the CPU time needed for the full set of Monte Carlo simulations is about 35[days] for $N_S = 5000$ realizations; see also Section 2.2).

Figure 6 juxtaposes analytical and numerical results describing the behavior of (normalized) longitudinal and transverse macrodispersion coefficients at increasing values of ${}^{r_1}/_{I_Y}$. Here, the analytical solution is compared against ensemble and effective numerical estimates, which are evaluated according to different calculation schemes (presented in the following) commonly employed in the literature (e.g., [37]).

Ensemble macrodispersion coefficients are evaluated along the directions parallel (i.e, $i = 1$) and perpendicular (i.e., $i = 2, 3$) to the mean flow as:

$$D_{ii}^{(ens)}(t) = \frac{1}{N_P}\sum_{j=1}^{N_P} D_{ii,j}^{(ens)}(t); \quad D_{ii,j}^{(ens)}(t) = \frac{1}{2}\frac{d}{dt}\left(\hat{\sigma}^2_{X_{i,j}}(t)\right)\Bigg|_t,$$

$$\text{with } i = 1, 2, 3, \quad j = 1, ..., N_P, \tag{22}$$

where $\hat{\sigma}^2_{X_{i,j}}(t)$ corresponds to the ensemble variance of the displacement of particle $j$ along direction $i$ evaluated across the collection of $N_S$ Monte Carlo realizations, at time $t$ (see Equation (D.3) in Supplementary Material D for details).

Effective macrodispersion coefficients are computed as:

$$D_{ii}^{(eff)}(t) = \frac{1}{N_S}\sum_{k=1}^{N_S} D_{ii,k}^{(eff)}(t); \quad D_{ii,k}^{(eff)}(t) = \frac{1}{2}\frac{d}{dt}\left(\hat{\sigma}^2_{X_{i,k}}(t)\right)\Bigg|_t,$$

$$\text{with } i = 1, 2, 3, \quad k = 1, ..., N_S, \tag{23}$$

where $\hat{\sigma}^2_{X_{i,k}}$ denotes the sample variance associated with the directional particle displacement of the plume in realization $k$ (see Equation (D.4) in Supplementary Material D for details).

Figure 6a shows that the numerically-based ensemble longitudinal macrodispersion exhibits an excellent agreement with its analytical counterpart for $\sigma_Y^2 = 1.684 \cdot 10^{-3}$. As expected, differences between analytical and numerical results are increasingly noticeable as $\sigma_Y^2$ increases. While longitudinal macrodispersion approaches a nearly horizontal (Fickian) asymptote at sufficiently late times/long distances for all levels of domain heterogeneity, the initial (pre-asymptotic) regime is characterized by a longer duration as $\sigma_Y^2$ increases and the asymptotic value increases with $\sigma_Y^2$. These features are ascribed to higher-order contributions which are not encapsulated in first-order analytical solutions.

The quality of the comparisons between numerical and analytical results associated with transverse macrodispersion (see Figure 6b) is similar to the one

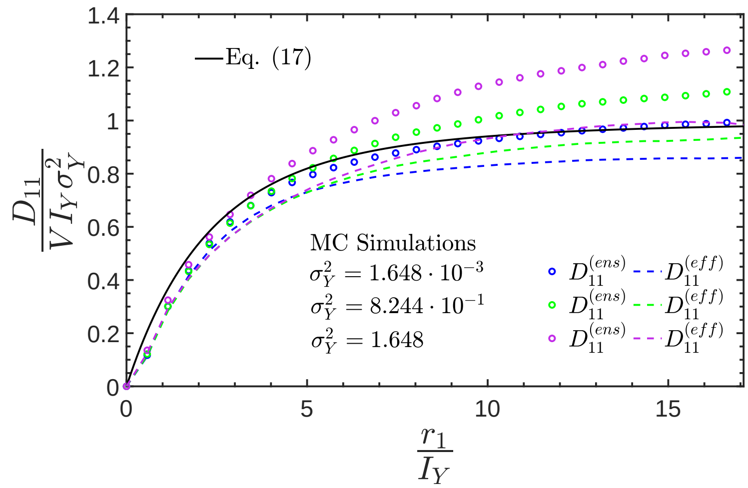


(a)

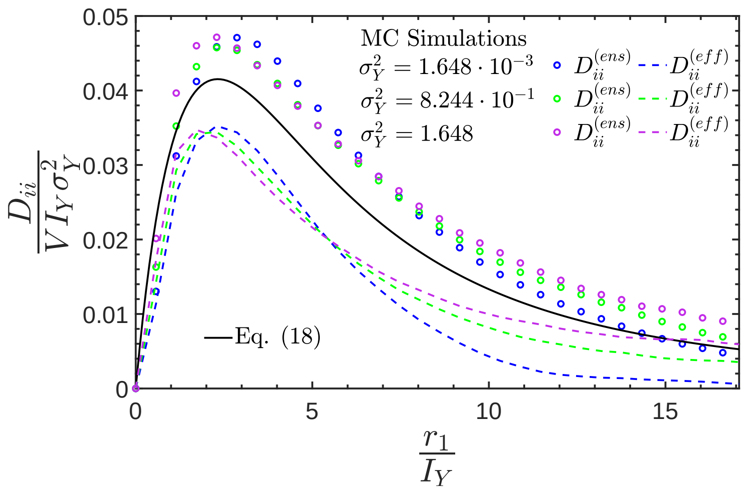


(b)

Figure 6: Normalized macrodispersion coefficients versus $\frac{r_1}{I_Y}$ along (a) longitudinal (i.e., along $i = 1$) and (b) transverse (i.e., along $i = 2, 3$) directions.

documented for its longitudinal counterpart. This is so even as the discrepancy between numerical (ensemble) and analytical values appears slightly less influenced by the value of $\sigma_Y^2$, the largest difference being about 14% in the cases here considered at ${}^{r_1}/_{I_Y} > 3$. Differences observed for the smallest heterogeneity (i.e., $\sigma_Y^2 = 1.684 \cdot 10^{-3}$) are due to the impact of boundary conditions, which can be mainly felt along the direction normal to the mean flow, as discussed above.

Figures 6a and 6b also enable one to visually appreciate that effective macrodispersion coefficients are always smaller than their ensemble counterparts. This observation is consistent with the definition of the two quantities considered, according to which $D_{ii}^{(eff)}$ represents a metric which quantifies the mean dispersion of a plume, while $D_{ii}^{(ens)}$ (with $i = 1, 2, 3$) is a measure of the mean degree of spreading of particles positions around the average plume position [37] (see also Supplementary Material D).

## 4. Summary, Remarks, and Conclusions

Our work provides an analytically-based assessment of the effect of non-Gaussian heterogeneous log-conductivity fields, $Y$, as captured by the Generalized Sub-Gaussian (GSG) model, on the key traits of flow and transport in three-dimensional settings. We focus on analytical expressions quantifying the spatial correlation of hydraulic head, seepage velocities, and particles displacements, to yield macrodispersion coefficients. An exponential correlation structure of $Y$ is considered for mathematical convenience to exemplify the key patterns of our solutions. The extension of the approach to include various functional formats of $C_Y$ could be the subject of future works. Our study leads to the following major conclusions:

- The covariance functions associated with hydraulic head and flow velocities are markedly affected by deviations of the log-conductivity of the host porous medium from the classical Gaussian model. This is manifest, e.g., through more persistent correlation structures of both head and velocity fields. The degree of correlation associated with the latter is markedly preserved at intermediate distances if compared against the classical Gaussian setting. Otherwise, such behavior persists at longer distances for directional head covariances. The spatial analysis of velocity fields is here limited to a standard covariance metric, which might lead to an overestimation of the level of correlation as compared to nonlinear indicators [9]. Quantification of the effects of the latter in GSG fields could reveal additional relevant information that will be addressed in future works.

- Analytical results about directional macrodispersion coefficients indicate that the GSG nature of $Y$ heavily influences pre-asymptotic dispersion values. This element appears to be markedly relevant if one considers that non-Fickian transport models have been widely developed in the literature upon resting on the assumption that a Gaussian model is representative of the spatial structure associated with underlying $Y$ fields [13, 14]. Our analyses suggest instead that the observed differences between GSG and Gaussian model-based scenarios may propagate to nonlinear mixing indicators [8], as these are known to be intrinsically linked to local transport features and particle transfer statistics. Late time conservative transport is always characterized by the attainment of a Fickian regime, a feature that appears independent of the degree of departure of the underlying domain from classical Gaussian structures.

- The main benefits of relying on analytical approaches (in this study and in general) is that they enable one to (1) enhance the current level of knowledge of the dynamics driving system evolution and (2) rigorously benchmark numerically based results. In this work, our analytical solutions also yield significant computational time/resources saving. Limitations of our results are related to the preliminary assumptions. Specifically, our analytical solution is consistent with numerical results related to sufficiently large domains (well approximating the assumption of infinite unbounded domain) and values of log-conductivity variances sufficiently smaller than unity.

- As expected, numerical estimates of the analyzed statistical moments are in good agreement with the analytical solutions when $\sigma_Y^2 << 1$, a scenario which fully satisfies the lead-order framework of analysis here considered. Therefore, our analytical expressions and results can also constitute a benchmark in the context of (stochastic) numerical analyses of flow and mass transport in heterogeneous porous media. Otherwise, numerical results suggest an increasingly significant role of higher-order terms at values of $\sigma_Y^2$ approaching or exceeding unity, a feature that cannot be captured considering only a first-order solution. Yet, the analytical solution can still capture the appropriate trend and order of magnitude of its (Monte Carlo-based) numerical counterparts even for the largest values of $\sigma_Y^2$ here considered (around 1.7). In this sense, reliance on our analytical approach is appealing because it enables one to grasp the effects of medium heterogeneity while favoring simplicity. As such, and along the lines of what has been suggested in previous works [41], it could be used to obtain prior information in preliminary analyses of solute plume evolution. This result is particularly relevant considering ($a$) the limited amount of information required by the analytical solution, ($b$) the limited loss of accuracy of the first-order solution at $\sigma_Y^2$ approaching or slightly exceeding unity, and ($c$) the significant computational and data management efforts associated with the implementation of a comprehensive Monte Carlo analysis across three-dimensional domains.

**Funding**

This research did not receive any specific grant from funding agencies in the public, commercial, or not-for-profit sectors.

## Acknowledgments

We acknowledge Professor Philippe Ackerer for sharing with us the codes employed for numerical flow simulation and particle tracking codes.

## References


[1] Dagan, G., 2012. Flow and transport in porous formations. Springer Science & Business Media.

[2] Zhang, D., 2001. Stochastic methods for flow in porous media: coping with uncertainties. Elsevier.

[3] Riva, M. and Guadagnini, A. and Fernandez-Garcia, D. and Sanchez-Vila, X. and Ptak, T, 2008. Relative importance of geostatistical and transport models in describing heavily tailed breakthrough curves at the Lauswiesen site. Journal of Contaminant Hydrology, 101 (1-4), 1–13, DOI: 10.1016/j.jconhyd.2008.07.004.

[4] Fiori, A. and Zarlenga, A. and Bellin, A. and Cvetkovic, V. and Dagan, G., 2019. Groundwater Contaminant Transport: Prediction Under Uncertainty, With Application to the MADE Transport Experiment. Frontiers in Environmental Science, 7, DOI: 10.3389/fenvs.2019.00079, ISSN: 2296-665X.

[5] Janetti, E. B. and Guadagnini, L. and Riva, M. and Guadagnini, A., 2019. Global sensitivity analyses of multiple conceptual models with uncertain parameters driving groundwater flow in a regional-scale sedimentary aquifer. Journal of Hydrology, 574, 544–556, Elsevier, DOI: 10.1016/j.jhydrol.2019.04.035.

[6] Janetti, E. B. and Riva, M. and Guadagnini, A., 2021. Natural springs protection and probabilistic risk assessment under uncertain conditions. Science of The Total Environment, 751, 141430, Elsevier, DOI: 10.1016/j.scitotenv.2020.141430.

[7] Li, K. and Wu, J. and Nan, T. and Zeng, X, 2022. Analysis of heterogeneity in a sedimentary aquifer using Generalized sub-Gaussian model based on logging resistivity. Stochastic Environmental Research and Risk Assessment, 36 (3), 767–783, DOI: 10.1007/s00477-021-02054-5.

[8] Le Borgne, T. and Dentz, M. and Villermaux, E., 2015.The lamellar description of mixing in porous media. Journal of Fluid Mechanics, 770, 458–498, Cambridge University Press, DOI: 10.1017/jfm.2015.117.

[9] Dell' Oca, A. and Porta, G., 2020. Characterization of flow through random media via Karhunen–Loéve expansion: an information theory perspective. GEM - International Journal on Geomathematics, 11 (18), DOI: 10.1007/s13137-020-00155-x.

[10] Comolli, A. and Hakoun, V. and Dentz, M., 2019. Mechanisms, Upscaling, and Prediction of Anomalous Dispersion in Heterogeneous Porous Media. Water Resources Research, 55 (10), 8197-8222, DOI: 10.1029/2019WR024919.

[11] Gotovac, H. and Cvetkovic, V. and Andricevic, R., 2009. Flow and travel time statistics in highly heterogeneous porous media. Water Resources Research, 45 (7), Wiley Online Library, DOI: 10.1029/2008WR007168.

[12] Di Dato, M. and D' Angelo, C. and Casasso, A. and Zarlenga, A., 2022. The impact of porous medium heterogeneity on the thermal feedback of open-loop shallow geothermal systems. Journal of Hydrology, 604, 127205, DOI: 10.1016/j.jhydrol.2021.127205, ISSN: 0022-1694.

[13] Edery, Y. and Guadagnini, A. and Scher, H. and Berkowitz, B., 2014. Origins of anomalous transport in heterogeneous media: Structural and dynamic controls. Water Resources Research, 50 (2), 1490–1505, Wiley Online Library, DOI: 10.1002/2013WR015111.

[14] Hansen, S. K. and Haslauer, C. P. and Cirpka, O. A. and Vesselinov, V. V., 2018. Direct Breakthrough Curve Prediction From Statistics of Heterogeneous Conductivity Fields. Water Resources Research, 54 (1) , 271–285, DOI: 10.1002/2017WR020450.

[15] Zech, A. and Attinger, S. and Bellin, A. and Cvetkovic, V. and Dagan, G. and Dentz, M. and Dietrich, P. and Fiori, A. and Teutsch, G., 2021. A Com-

parison of Six Transport Models of the MADE-1 Experiment Implemented With Different Types of Hydraulic Data. Water Resources Research, 57 (5), e2020WR028672, DOI: 10.1029/2020WR028672.

[16] Xu, W. and Liang, Y. and Chen, W. and Cushman, J. H., 2019. A spatial structural derivative model for the characterization of superfast diffusion/dispersion in porous media. International Journal of Heat and Mass Transfer, 139, 39–45, DOI: 10.1016/j.ijheatmasstransfer.2019.05.001, ISSN: 0017-9310.

[17] Park, B.H. and Lee, K.K., 2021. Evaluating anisotropy ratio of thermal dispersivity affecting geometry of plumes generated by aquifer thermal use. Journal of Hydrology, 602, 126740, DOI: 10.1016/j.jhydrol.2021.126740, ISSN: 0022-1694.

[18] Sole-Mari, G. and Riva, M. and Fernàndez-Garcia, D. and Sanchez-Vila, X. and Guadagnini, A., 2021. Solute transport in bounded porous media characterized by generalized sub-Gaussian log-conductivity distributions. Advances in Water Resources, 147, 103812, DOI: 10.1016/j.advwatres.2020.103812, ISSN: 0309-1708.

[19] de Barros, F. P. J. and Guadagnini, A. and Riva, M., 2022. Features of transport in non-Gaussian random porous systems, International Journal of Heat and Mass Transfer, 184, DOI: 10.1016/j.ijheatmasstransfer.2021.122244.

[20] Severino, G., 2022. Dispersion in doublet-type flows through highly anisotropic porous formations. Journal of Fluid Mechanics, 931, A2, Cambridge University Press, DOI: 10.1017/jfm.2021.929.

[21] Gelhar, L. W., 1993. Stochastic subsurface hydrology. Prentice-Hall.

[22] Siena, M. and Guadagnini, A. and Riva, M. and Neuman, S., 2012. Extended power-law scaling of air permeabilities measured on a block of tuff.

Hydrology and Earth System Sciences, 16 (1), 29–42, Copernicus GmbH, DOI: 10.5194/hess-16-29-2012.

[23] Painter, S., 1996. Evidence for non-Gaussian scaling behavior in heterogeneous sedimentary formations. Water Resources Research, 32 (5), 1183–1195, Wiley Online Library, DOI: 10.1029/96WR00286.

[24] Siena, M. and Riva, M. and Giamberini, M. and Gouze, P. and Guadagnini, A., 2019. Statistical modeling of gas-permeability spatial variability along a limestone core. Spatial Statistics, 34, 100249, Elsevier, DOI: 10.1016/j.spasta.2017.07.007.

[25] Riva, M. and Neuman, S. P. and Guadagnini, A., 2013. Sub-Gaussian model of processes with heavy-tailed distributions applied to air permeabilities of fractured tuff, Stochastic Environmental Research and Risk Assessment, 27 (1) , 195–207, Springer, DOI: 10.1007/s00477-012-0576-y.

[26] Riva, M. and Neuman, S. P. and Guadagnini, A. and Siena, M., 2013. Anisotropic scaling of Berea sandstone log air permeability statistics. Vadose Zone Journal, 12 (3), GeoScienceWorld, DOI: 10.2136/vzj2012.0153.

[27] Painter, S., 2001. Flexible scaling model for use in random field simulation of hydraulic conductivity. Water Resources Research, 37 (5), 1155–1163, Wiley Online Library, DOI: 10.1029/2000WR900394.

[28] Yang, C. and Hsu, K. and Chen, K., 2009. The use of the Levy-stable distribution for geophysical data analysis. Hydrogeology Journal, 17 (5), 1265–1273, Springer, DOI: 10.1007/s10040-008-0411-1.

[29] Guadagnini, A. and Neuman, S. P. and Schaap, M. and Riva, M., 2014. Anisotropic statistical scaling of soil and sediment texture in a stratified deep vadose zone near Maricopa, Arizona. Geoderma, 214, 217–227, Elsevier, DOI: 10.1016/j.geoderma.2013.09.008.

[30] Siena, M. and Guadagnini, A. and Bouissonnié, A. and Ackerer, P. and Daval, D. and Riva, M., 2020. Generalized sub-Gaussian processes: The-

ory and application to hydrogeological and geochemical data. Water Resources Research, 56 (8), e2020WR027436, Wiley Online Library, DOI: 10.1029/2020WR027436.

[31] Riva, M. and Neuman, S. P. and Guadagnini, A., 2015. New scaling model for variables and increments with heavy-tailed distributions. Water Resources Research, 51 (6), 4623–4634, Wiley Online Library, DOI: 10.1002/2015WR016998.

[32] Riva, M. and Guadagnini, A. and Neuman, S. P., 2017. Theoretical analysis of non-Gaussian heterogeneity effects on subsurface flow and transport. Water Resources Research, 53 (4), 2998–3012, Wiley Online Library, DOI: 10.1002/2016WR019353.

[33] Guadagnini, A. and Riva, M. and Neuman, S. P., 2018. Recent advances in scalable non-Gaussian geostatistics: The generalized sub-Gaussian model. Journal of hydrology, 562, 685–691, Elsevier, DOI: 10.1016/j.jhydrol.2018.05.001.

[34] Libera, A. and de Barros, F. P. J. and Riva, M. and Guadagnini, A., 2017. Solute concentration at a well in non-Gaussian aquifers under constant and time-varying pumping schedule. Journal of contaminant hydrology, 205, 37–46, Elsevier, DOI: 10.1016/j.jconhyd.2017.08.006.

[35] Ababou, R., 1988. Three-dimensional flow in random porous media. PhD Thesis, Massachusetts Institute of Technology.

[36] Panzeri, M. and Riva, M. and Guadagnini, A. and Neuman, S. P., 2016. Theory and generation of conditional, scalable sub-Gaussian random fields. Water Resources Research, 52 (3), 1746–1761, Wiley Online Library, DOI: 10.1002/2015WR018348.

[37] de Dreuzy, J.-R. and Beaudoin, A. and Erhel, J., 2007. Asymptotic dispersion in 2D heterogeneous porous media determined by parallel numeri-

cal simulations. Water Resources Research, 43 (10), Wiley Online Library, DOI: 10.1029/2006WR005394.

[38] Beaudoin, A. and de Dreuzy, J.-R., 2013. Numerical assessment of 3-D macrodispersion in heterogeneous porous media. Water Resources Research, 49 (5), 2489–2496, Wiley Online Library, DOI: 10.1002/wrcr.20206.

[39] Winter, T. C., 2003. Hydrological, chemical, and biological characteristics of a prairie pothole wetland complex under highly variable climate conditions: the Cottonwood Lake area, east-central North Dakota. US Department of the Interior, US Geological Survey, 1675, DOI: 10.3133/PP1675.

[40] Riva, M. and Guadagnini, A. and Neuman, S. P. and Franzetti, S., 2001. Radial flow in a bounded randomly heterogeneous aquifer. Transport in Porous Media, 45 (1), 139–193, Springer, DOI: 10.1023/A:1011880602668.

[41] de Barros, F.P.J. and Fiori, A., 2014. First-order based cumulative distribution function for solute concentration in heterogeneous aquifers: Theoretical analysis and implications for human health risk assessment. Water Resources Research, 50 (5), 4018–4037, Wiley Online Library, DOI: 10.1002/2013WR015024.

[42] Dejam, M., 2019. Advective-diffusive-reactive solute transport due to non-Newtonian fluid flows in a fracture surrounded by a tight porous medium. International Journal of Heat and Mass Transfer, 128, 1307–1321, DOI: 10.1016/j.ijheatmasstransfer.2018.09.061.

[43] Dai, Z. and Zhan, C. and Dong, S. and Yin, S. and Zhang, X. and Soltanian, M. R., 2020. How does resolution of sedimentary architecture data affect plume dispersion in multiscale and hierarchical systems?. Journal of Hydrology, 582, 124516, DOI: 10.1016/j.jhydrol.2019.124516

Figure 1 .tif

Click here to access/download;Figure;Flow chart.tif

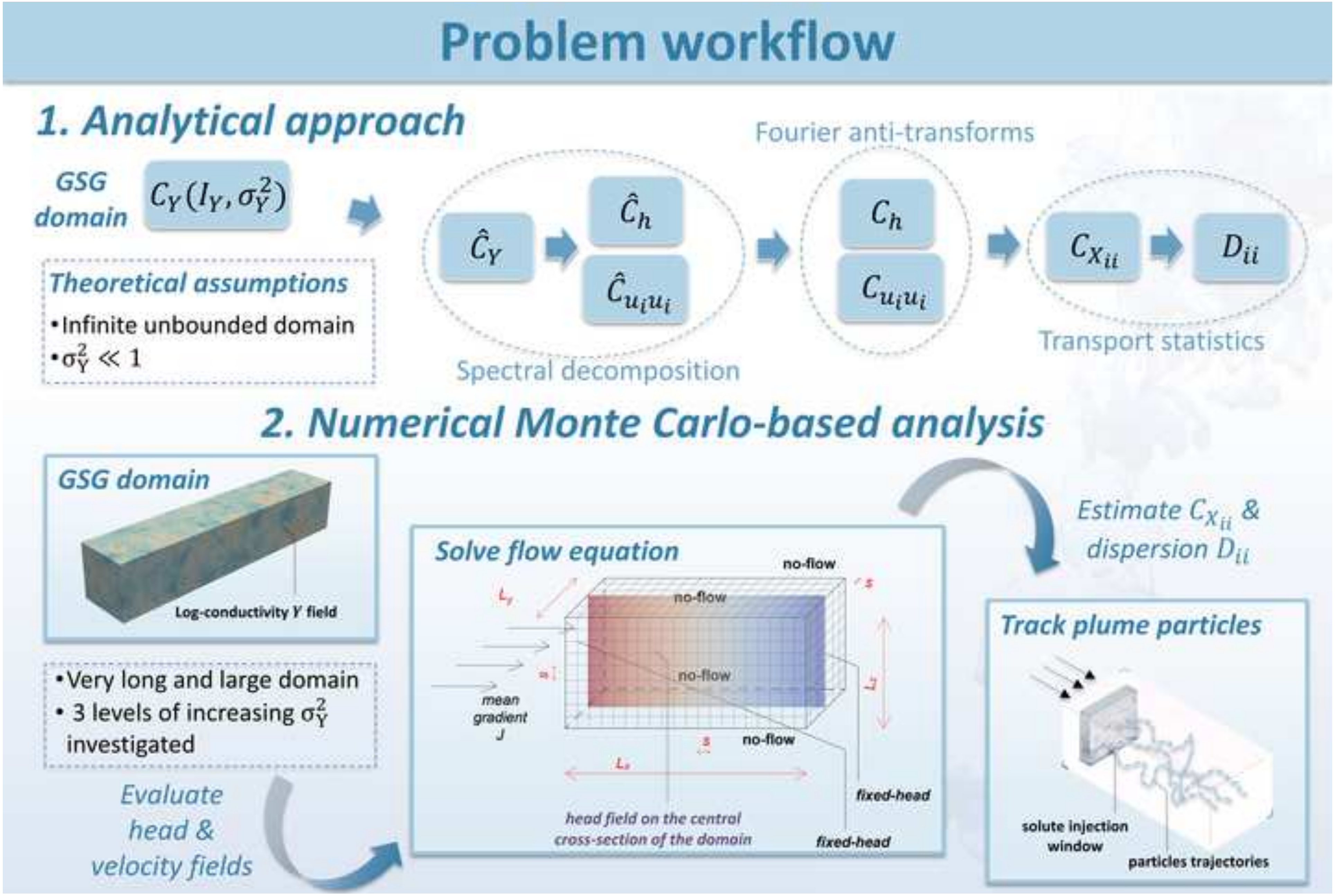

Figure 2 .tif

Click here to access/download;Figure;domain.tif

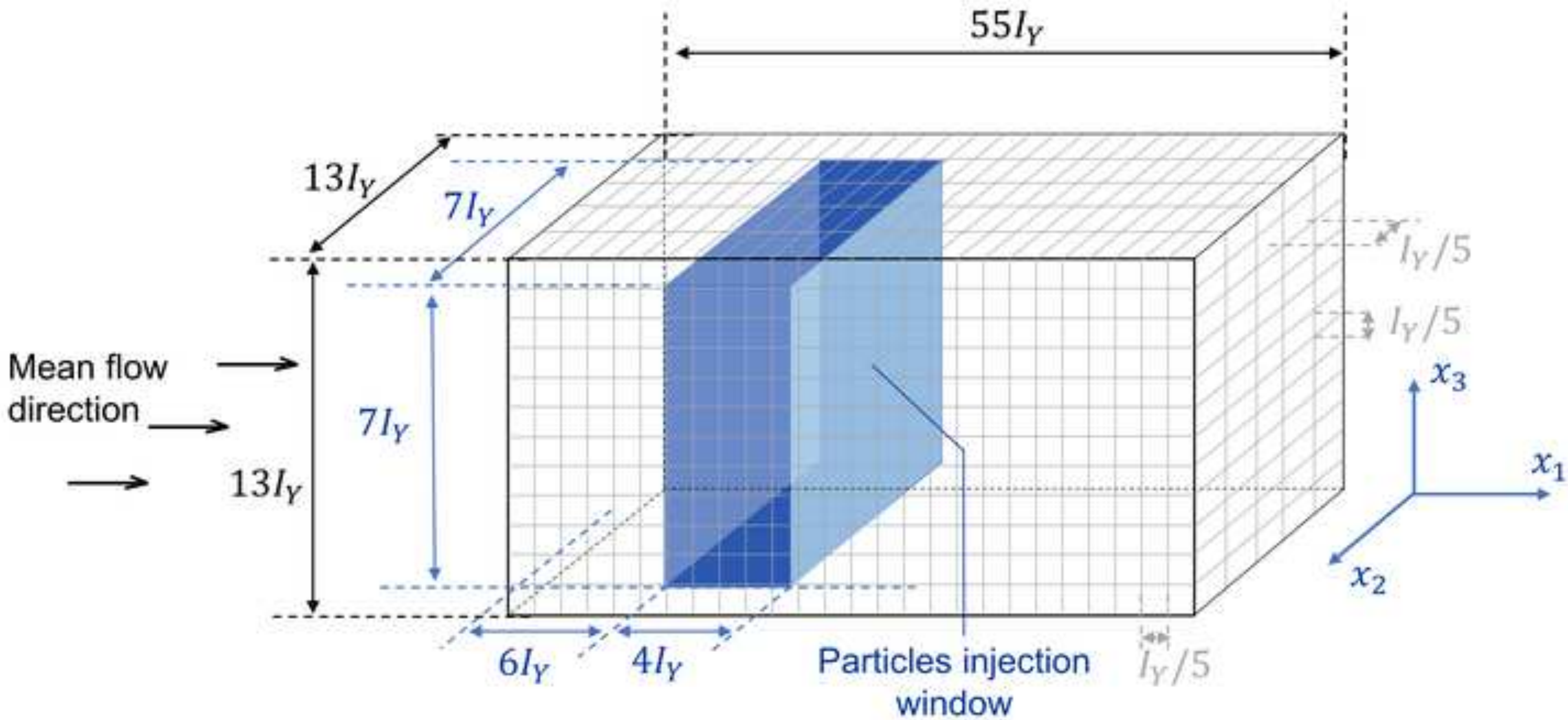

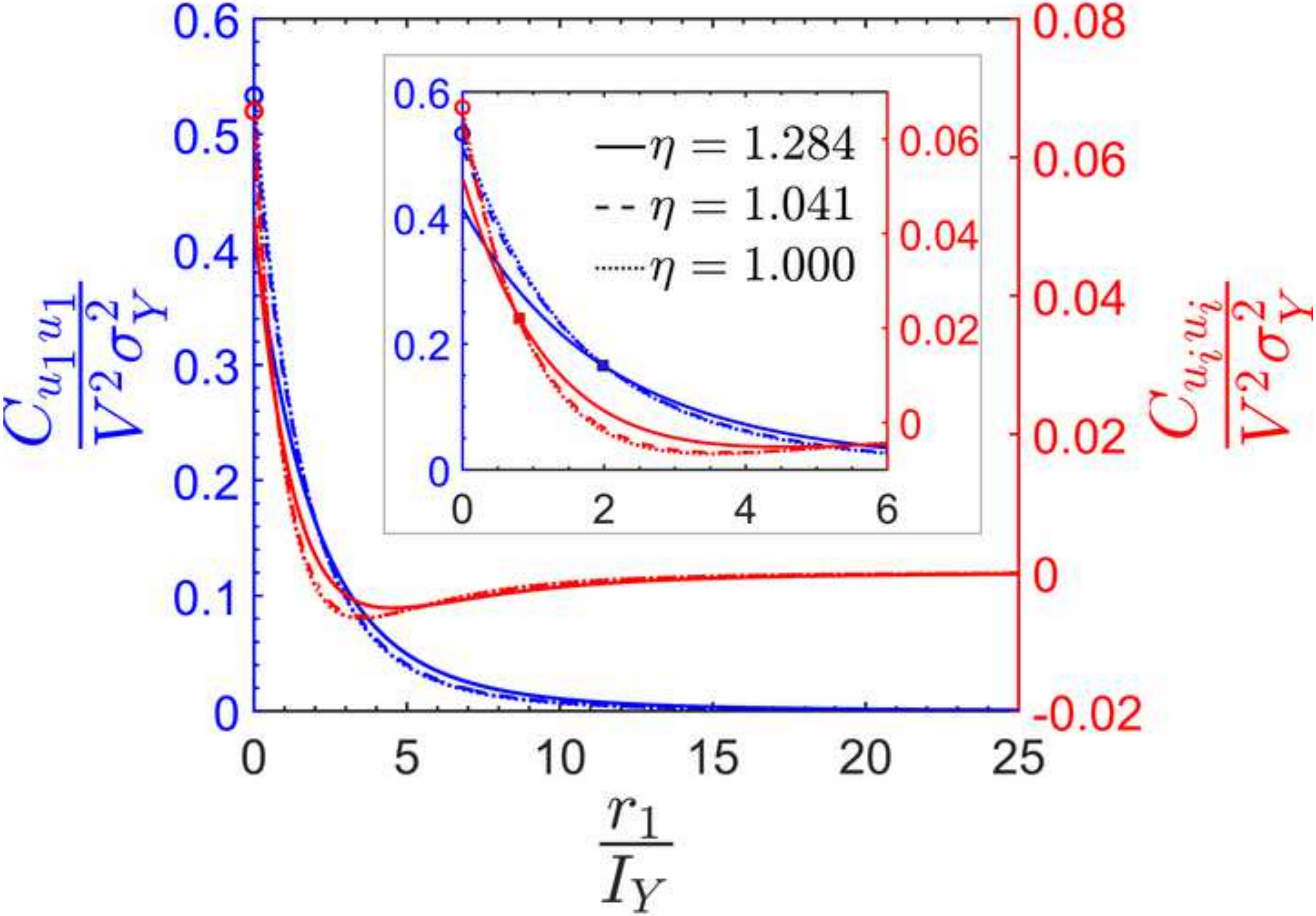
0.6
0.5
0.4
0.3
0.2
0.1
0
0.08
0.06
0.04
0.02
0
-0.02
0
5
10
15
20
25
$\frac{C_{u_1u_1}}{V^2\sigma_Y^2}$
$\frac{C_{u_iu_i}}{V^2\sigma_Y^2}$
$\frac{r_1}{I_Y}$
0.6
0.4
0.2
0
0.06
0.04
0.02
0
0
2
4
6
$\eta = 1.284$
$\eta = 1.041$
$\eta = 1.000$

Click here to access/download
**Supplementary Material**
SMs.pdf